### FUTURES ISSUE: SEPARATIONS: MATERIALS, DEVICES AND PROCESSES

AICHE TOURNAL

Check for updates

# Lanthanum induced lattice strain improves hydrogen sulfide capacities of copper oxide adsorbents

Griffin A. Canning<sup>1,2</sup> | Sara A. Azzam<sup>3</sup> | Adam S. Hoffman<sup>4</sup> | Alexey Boubnov<sup>4</sup> | Faisal H. Alshafei<sup>3</sup> | Richa Ghosh<sup>3</sup> | Brian Ko<sup>3</sup> | Abhaya Datye<sup>1,2</sup> | Simon R. Bare<sup>4</sup> | Dante A. Simonetti<sup>3</sup>

### Correspondence

Dante A. Simonetti, Chemical and Biomolecular Engineering Department, University of California-Los Angeles, Los Angeles, CA 90095, USA. Email: dasimonetti@ucla.edu

Simon R. Bare, Stanford Synchrotron Radiation Lightsource, SLAC National Accelerator Laboratory, Menlo Park, California, USA. Email: dasimonetti@ucla.edu

### **Funding information**

American Chemical Society Petroleum Research Fund, Grant/Award Number: 56978-DNI5; Basic Energy Sciences, Grant/ Award Number: DE-AC02-76SF00515; National Science Foundation, Grant/Award Number: EEC-1647722 (CISTAR); The American Chemical Society Petroleum Research Fund; Office of Equity, Diversity, and Inclusion at UCLA; UCLA Samueli School of Engineering

#### **Abstract**

This work probes the effects of La on reactions involving CuO sorbents and  $H_2S$  in gaseous streams. La-CuO sorbents with nominal La/Cu atomic ratios of 1:2 achieved higher capacities (27 and 36 g  $H_2S$  per 100 g sorbent) compared to CuO sorbents (25 g  $H_2S$  per 100 g sorbent). Comparison of the La-CuO sorbents using energy dispersive x-ray spectroscopy and La  $L_3$ -edge XAS suggested that increased capacity resulted from more uniform dispersion of La within the CuO phase (3.3 wt.% vs. 1.0 wt.% La). X-Ray absorption near edge structure analysis suggested more electron-rich Cu species in La-CuO samples, while extended X-ray absorption fine structure modeling showed an increase in single-scattering path lengths for neighboring and near-neighbor atoms. These changes suggest that La induces strain in the Cu-O lattice, thereby increasing  $H_2S$  capacity by reducing energy barriers associated with surface reactions between oxygen atoms and adsorbed  $H_2S$  molecules.

### **KEYWORDS**

copper oxide, desulfurization, doping, lanthanum oxide, reactive sorption, X-ray absorption spectroscopy

### 1 | INTRODUCTION

The total global energy demand for natural gas, driven by population growth and technology development, is projected to increase by 43%

in the coming two decades.<sup>1</sup> This increase in energy consumption, along with an increase in environmental regulations, calls for enhancing current gas purification technologies to be cleaner and more efficient.<sup>2</sup> Raw natural gas contains significant amounts of sulfur contaminants which reduce its quality,<sup>3–5</sup> corrode transfer pipelines, damage catalysts and process equipment, and pose toxic hazard to

Griffin A. Canning and Sara A. Azzam contributed equally to this study.

AIChE J. 2021;67:e17484. https://doi.org/10.1002/aic.17484

<sup>&</sup>lt;sup>1</sup>Department of Chemistry and Chemical Biology, University of New Mexico, Albuquerque, New Mexico, USA

<sup>&</sup>lt;sup>2</sup>Department of Chemical and Biological Engineering, University of New Mexico, Albuquerque, New Mexico, USA

<sup>&</sup>lt;sup>3</sup>Chemical and Biomolecular Engineering Department, University of California-Los Angeles, Los Angeles, California, USA

<sup>&</sup>lt;sup>4</sup>Stanford Synchrotron Radiation Lightsource, SLAC National Accelerator Laboratory, Menlo Park, California, USA

humans and to the environment.<sup>6</sup> Many technologies are currently available for sulfur removal including absorptive processes (e.g., amine scrubbing), adsorptive processes (e.g., using molecular sieves), and chemical reactions (e.g., using metal oxides).<sup>7–9</sup> For trace levels of these sulfur contaminants (i.e., less than a few ppm), chemical reaction with a metal oxide (also known as reactive sorption) is advantageous compared to physisorption because the favorable thermodynamics of these reactions allow for essentially complete removal of the contaminant. Moreover, the process converts toxic reactants to environmentally benign metal sulfide products.<sup>10</sup>

The materials studied previously for reactive sorption of hydrogen sulfide (H<sub>2</sub>S) consist mostly of the oxides, hydroxides, and carbonates of iron, zinc, and copper at 473-1073 K.11-13 Elevated process temperatures are used to mitigate the kinetic limitations encountered at low temperature which result in low utilization factors. 12,14 Among these materials, copper oxides (CuO and Cu2O) are considered the most favorable sorbents for sulfur removal. A comprehensive thermodynamic study of the copper-sulfur-oxygen system<sup>15</sup> show high equilibrium constants (e.g.,  $K_{\text{eq}} = 6.3 \, \times 10^{17} \, \text{at 900 K)}$  which result in a decrease in H<sub>2</sub>S concentration from several thousand ppm to the subppm concentrations. Nevertheless, CuO is susceptible to reduction to metallic copper (Cu) at high temperatures, leading to agglomeration and structural degradation which inhibits contaminant sorption rates and kinetics. 16 Thus, additives are often added to CuO (e.g., ZnO) in an effort to stabilize Cu<sup>2+</sup> and Cu<sup>1+</sup> against reduction to Cu, thereby improving sulfur removal capacities and rates. 17-18 Similar studies of mixed metal oxides at ambient temperature also demonstrated the benefits of metal additives on H<sub>2</sub>S removal capacity, suggesting that the impact of these additives may extend beyond improving reduction resistance. 19-22

To probe how the structural and chemical changes incurred by introducing metal atoms into CuO impact reactions with H<sub>2</sub>S at the molecular/atomic scale, advanced characterization techniques must be utilized in addition to reaction studies. In our previous work, the effects of crystallite size and micro-porosity on the performance of chemically similar CuO sorbents were investigated using a combination of reaction studies, advanced characterization techniques such as x-ray absorption spectroscopy (XAS), and density functional theory (DFT).<sup>23-25</sup> These studies showed that the observed increase in H<sub>2</sub>S capacity with decreasing CuO crystallite size could be the result of a higher density of threefold coordinated oxygen atoms within small CuO crystallites that are more reactive toward adsorbed H<sub>2</sub>S molecules (i.e., for bulk reactions  $CuO + xH_2S \rightarrow CuO_{1-x}S_x + xH_2O$ ) compared to fourfold atoms. These threefold coordinated O-atoms also form vacancies in the CuO surface more readily (i.e., via formation of hydroxyl groups with reaction with adsorbed H-atoms) than fourfold sites. Importantly, this work showed that fourfold sites actually become increasing reactive as CuO converts to CuS because S atoms induce lattice strain by disrupt the Cu-O bonding states. Furthermore, our previous work also showed that the formation of thermodynamically favorable, surface-strained Cu-S bonds stabilize surface hydroxyl groups, thereby reducing barriers toward reaction and migration.

In this work, we study the impact of induced strain via addition of lanthanum (La) on the structural properties and sulfur removal performance of CuO through a combination of fixed-bed kinetic studies and synchrotron-based characterization techniques. La was chosen because of its large cationic radius ( $R_{La}/R_{Cu}\approx 1.5$ ) compared to the more commonly studied additives such as zinc, nickel and cobalt ( $R_x$ / $R_{Cu}\approx 1.0$ ). This difference in cationic radius is expected to introduce disruptions to the CuO lattice,  $^{23,26}$  which would cause the formation of O-atoms that are more reactive with adsorbed surface species,  $^{27}$  similar to previous studies that have found similar disruptions to the ([Mn, Zn]Fe $_2$ O $_4$ , ZnMnO $_3$ ) lattice by the presence of Mn increases the sulfur sorption of a Fe-Mn-Zn-Ti mixed oxide.  $^{28}$ 

To explore the structural and chemical changes upon lanthanum addition, we collected X-ray absorption spectroscopy (XAS) spectra for fresh and spent reference commercial CuO-based sorbent and laboratory-synthesized La-CuO sorbents (1:2 nominal La to Cu atomic ratio) prepared by different synthesis methods (sol-gel and coprecipitation with ammonium). XAS data were collected at the S K-. Cu K-, and La L<sub>3</sub>-edges to provide complimentary evidence of the chemical and structural differences between the samples. In situ X-ray absorption near edge spectroscopy (XANES) data at the S K-edge were collected for the three samples using 1000 ppm H<sub>2</sub>S/He, 1 atm, and 323 K. The resulting kinetic rate information that was directly related to structural changes was consistent with fixed-bed reactor results. Additionally, X-ray diffraction (XRD), N<sub>2</sub>-physisorption measurements (BET), scanning electron microscopy (SEM), transmission electron microscopy (TEM), and energy-dispersive x-ray spectroscopy (EDS) were used to form a chemical and structural analysis of the samples.

### 2 | EXPERIMENTAL METHODS

### 2.1 | Materials

Several CuO and La-CuO materials at various La:Cu ratios were prepared using an acid catalyzed sol-gel synthesis technique or a method of coprecipitation. Section 1.1 in the supplementary information (SI) provides synthesis details of these samples as well as naming conventions. The main text of this article focuses on one CuO-based sample (CuO-1), and two CuO samples with La synthesized with a nominal La:Cu molar ratio of 1:2 (CuO-La-1 and CuO-La-2). Other synthetic conditions (CuO-La-3 thru 5) produced less performance improvement upon La inclusion and are discussed in the Supplemental Information.

CuO-1 is a commercially produced material (HiFUEL W230; lot number L04Y006; 63.5 wt.% CuO, 25 wt.% ZnO, and 10 wt.% Al $_2$ O $_3$ ) purchased from Alfa Aesar. This sample was used as a reference for comparison with the lanthanum containing samples and was studied in previous work.  $^{23,24}$ 

CuO-La-1 was prepared using an acid-catalyzed sol-gel process.<sup>29</sup> 1.0 cm<sup>3</sup> of glacial acetic acid (VWR, ACS grade) was added to 300 cm<sup>3</sup> of 0.133 M copper (II) nitrate (Sigma Aldrich, 99%) and

tions) on Wiley Online Library for rules of use; OA articles are governed by the applicable Creative Commons

CANNING ET AL.

AICHE 3 of 10

0.067 M lanthanum (III) nitrate hexahydrate (Sigma Aldrich, 99%) under vigorous stirring and heating. Upon boiling, 0.8 g of sodium hydroxide was added to the solution with continuous stirring, creating a precipitate. The supernatant was then poured off and the precipitate was washed with deionized water and ethanol (Sigma-Aldrich, 100%). The washed precipitate was then dried in air for 24 h at 333 K. A reference  $La_2O_3$  material was synthesized by the same method using only lanthanum (III) nitrate hexahydrate.

CuO-La-2, sample was synthesized via an aqueous ammonia coprecipitation method.<sup>30</sup> 1.0 cm<sup>3</sup> of ammonium hydroxide (Fisher Scientific, ACS Plus) was added dropwise to 300 cm<sup>3</sup> of aqueous 0.133 M copper (II) nitrate and 0.067 M lanthanum (III) nitrate hexahydrate solution until a precipitate formed. The precipitate was then allowed to settle, and the effluent was decanted. The sample was then washed and centrifuged twice, dried in a drying oven (353 K) overnight, and thermally treated at 873 K for 2 h, afterward.

### 2.2 | Fixed-bed sulfidation tests

Fixed-bed sorption experiments were carried out in a plug flow apparatus shown schematically in Figure S1.31 A 0.25-inch outer diameter tubular stainless-steel reactor was packed with 100-180 mg of material that was sieved to 75-125 μm particle sizes. The packed beds were 1.4-1.9 cm in height and were fixed between two plugs of quartz wool. The temperature of the reactor was set to 323 K and was regulated using a resistively heated jacket with a PID temperature controller (TEMPCO EPC-100). The inlet flow composition to the reactor consisted of 1000 ppm-vol H<sub>2</sub>S in N<sub>2</sub> (produced by diluting 1.0% H<sub>2</sub>S/N<sub>2</sub> [Praxair] in UHP N<sub>2</sub>). The total inlet flow rate of 90 sccm was controlled using MKS GE50A and GM50A flow controllers. An online gas chromatograph (Agilent 7890B) with a sulfur chemiluminescence detector (SCD; Agilent 755) was used to measure the concentration of sulfur in inlet and outlet streams. The interior of the reactor and all the gas transfer lines were treated by an inert coating (SilcoNert 2000) to mitigate adsorption of sulfur onto the apparatus flow path walls.

### 2.3 | Nonsynchrotron characterization techniques

The sorbents were characterized using a variety of techniques. Powder XRD patterns were obtained using either a JEOL JDX-3530, a Philips X-Pert diffractometer, or a Rigaku Smart Lab Diffractometer equipped with a D/teX position sensitive detector with a nickel filter using Cu  $\rm K\alpha$  radiation (1.5410 Å) to identify the crystalline phases. Average crystallite sizes were determined using whole-pattern Rietveld refinement by the Jade software package from Materials Data, Inc. Nitrogen adsorption–desorption isotherms were measured at 77 K with a Micrometrics ASAP 2020 Plus system. Before measurements, the samples were degassed at  $1\times 10^{-3}$  Torr and 573 K. The Brunauer–Emmett–Teller (BET) surface areas were calculated from the isotherms by using the BET equation. The pore size distribution

was derived from the adsorption branches of the isotherms using the Barrett-Joyner-Halenda model.

SEM (NOVA 230 Nano SEM) was used to determine the morphology of the sorbents. The diameter of the sorbent particles was calculated from the SEM images using the ImageJ software. For TEM analysis, the powdered sample was ground in a mortar and pestle and dispersed on a holey carbon grid by dry impregnation. Two different TEMs were used to obtain images for the samples. The first, a FEI Tecnai G (2) F30 S-Twin operated at 300 kV; and the second, a JEOL 2010F 200 kV equipped with an Oxford AZTEC 80 mm<sup>2</sup> SDD EDS detector with an ultrathin window. STEM imaging was performed on the Tecnai F30, TEM imaging and selected area EDS was performed on the JEOL 2010F. In this technique, the microscope is operated in TEM mode, and the beam condensed at higher spot sizes and a condenser aperture is inserted in order to limit the field of excitation to key areas of interest. This technique was used in place of STEM-EDS mapping due to the beam sensitivity of copper oxide materials.<sup>32</sup> For this study, areas of interest were smaller clusters of crystallitestypically on the order of 50-100 nm. EDS spectra were collected at 8-10 spots to obtain an average elemental composition for each sample.

### 2.4 | Synchrotron-based characterization

XAS spectra were recorded at the Stanford Synchrotron Radiation Lightsource (SSRL) at wiggler beamline 4–3 using a liquid-nitrogen cooled. Si(111) double-crystal monochromator. The storage ring was operated at 3 GeV with a ring current of 494–500 mA in top-up mode. The beam cross-section was 1 mm vertical x 3 mm horizontal. XANES spectra were recorded at the S K-edge (2472 eV) and La  $L_3$ -edge (5483 eV) in fluorescence mode using a 7-element silicon-drift detector (Canberra) and full extended X-ray absorption fine structure (EXAFS) at the Cu K-edge (8979 eV) in transmission mode.

The sample for XAS experiments comprised a non-self-supporting wafer consisting of 36 mg of CuO-based sample mixed with 14 mg of boron nitride (BN) (Sigma Aldrich) for the S K-edge, and 2.4 mg of sample diluted with 47.6 mg BN for the Cu K-edge and La  $L_3$ -edge. The wafer was placed at  $45^{\circ}$  to the incident beam on a heated stage inside a  $100 \text{ cm}^3$  internal volume cell, as described previously and as shown in Figure S2.<sup>33</sup> The experimental cell was connected to the  $I_0$  ion chamber and beam conditioning assembly through a welded steel bellows and KF flanges. Helium from the  $I_0$  ion chamber was allowed to purge the bellows to reduce adsorption by heavier gases in the beam path. A five micron mylar film was placed between the KF flanges and O-ring of the experimental cell and the welded bellows to isolate the process gas from the ion chamber and purge gas.

For XAS monitoring of *in situ* sulfidation experiments at the S K-edge, 1000 ppm  $H_2S$  in helium (Airgas) and helium (99.95%, Airgas) gases were used. All process gases were supplied by Airgas with a purity of 99.5% or higher for each component. No further purification was performed to remove trace moisture of oxygen. Effluent gas from the experimental cell was monitored by mass spectrometry (MS) using

15475905, 2021, 12, Downloaded from https://aiche.onlinelibrary.wiley.com/doi/10.1002/aic.17484 by Purdue University (West Lafayette), Wiley Online Library on [10/07/2023]. See the Terms itions) on Wiley Online Library for rules of use; OA articles are governed by the applicable Creative Commons

a Hiden QGA. Prior to experiments, the cell was leak checked and purged with each feed component until all signals in the MS were stable. Care was taken to check for air leaks by monitoring m/z signals of 18, 28, and 32 corresponding to  $H_2O$ ,  $N_2$ , and  $O_2$  in the stream. Additionally, the MS was used to ensure that  $H_2S$  was purged before accessing the cell as well as confirming the lack of air leaks. Initially, the temperature of the cell is ramped up to 323 K at a ramp rate of  $5 \text{ K·min}^{-1}$  under a 20 sccm flow of helium. Once temperature stabilized, the helium was replaced with 1000 ppm  $H_2S/He$  (20 sccm) and XANES spectra collected every 9 min. The samples were exposed to 1000 ppm  $H_2S/He$  flow for 4–6 h until saturation was achieved. The cell was then purged by helium (20 sccm) and allowed to cool to room temperature before spectra of spent samples were obtained.

XAS data were analyzed using ATHENA and ARTEMIS from the Demeter software package. The Cu K-edge EXAFS data were extracted from a k-range of 3.0–13.0 Å $^{-1}$ , and the Fourier transformed data were modeled in the range of 1.0–3.2 Å. Intensity and phase of scattering paths were calculated using FEFF6 based on crystallographic data from the tenorite CuO structure (ICSD 16025). EXAFS fitting was performed based on k-, k-, and k-weighting. S $_0$ 2 was determined to be 0.73 for these samples based on fitting a reference copper foil with tabulated coordination numbers (fcc-Cu metal: ICSD 53247). f

### 3 | RESULTS AND DISCUSSION

### 3.1 | Effects of nominal La content and synthesis method on removal capacity

Initial H<sub>2</sub>S removal studies were conducted for La-CuO sorbents for various nominal La:Cu atomic ratios (1:99, 1:9, 1:2) using fixed-bed experiments at 323 K to probe the impact of La content and synthesis method. The removal capacity ( $q_s$ ) is defined as g of H<sub>2</sub>S removed per 100 g of CuO in the sorbent (g H<sub>2</sub>S/100 g CuO), with  $q_s = 42$  g H<sub>2</sub>S/100 g CuO corresponding to complete stoichiometric conversion of CuO to CuS.

Table S1 summarizes the synthesis conditions, nominal La/Cu atomic ratio in the synthesis precursors, crystallite size, removal capacities, and conversion of CuO phase for all the tested samples. For different CuO samples (CuO-1 through CuO-3), capacities decreased (from 24.9 to 20.4 g  $H_2S/100$  g CuO) with increasing CuO crystallite size (from 2.8 to 8.0 nm), consistent with results from prior research. The removal capacity of the La<sub>2</sub>O<sub>3</sub> sample (determined using the same fixed-bed experiments) was negligible ( $\sim$ 0.005 g  $H_2S$  per g La<sub>2</sub>O<sub>3</sub>), demonstrating that CuO and La-CuO are the only active phases in these samples.

Moderate amounts of La addition (CuO-La-4; La:Cu = 1:9; CuO crystallite size of 8 nm) lead to a decrease in capacity (13 g  $\rm H_2S/100$  g CuO) compared to CuO samples synthesized via similar methods and with similar crystallite size (CuO-3; 20.4 g  $\rm H_2S/100$  g CuO). However, capacities increased with increasing La content such that La-CuO samples with atomic La:Cu ratios of 1:2 achieved capacities (CuO-La-1: 26.9 g  $\rm H_2S/100$  g CuO and CuO-La-2: 35.8 g  $\rm H_2S/100$  g CuO)

that were greater than CuO samples, despite the presence of larger CuO crystallites (CuO-La-1: 15.9 nm and CuO-La-2: 42.2 nm). Furthermore, La-containing samples appear to no longer follow the typical capacity-crystallite size trend (increasing capacity with decreasing size) established in our previous work.<sup>23</sup> The synthesis method also appears to impact sorption capacity, with the sample prepared using aqueous ammonia (CuO-La-2) achieving higher sorption capacity than those made by the sol-gel or coprecipitation methods. These results suggest that increasing inclusion of La into the CuO phase improves total sulfur sorption and that synthesis method (i.e., La content in solution and pH) is a key factor toward ensuring incorporation of La atoms into the CuO sample. Precipitation at lower pH (i.e., in aqueous ammonia) slows the precipitation of La<sub>2</sub>O<sub>3</sub> phases, thereby allowing a larger extent of incorporation into Cu-La-O.30 To quantify any incorporation of La into the CuO lattice, and further explore the structural and electronic effects of introducing La into CuO sorbents, CuO-La-1 and CuO-La-2 were thoroughly characterized to identify the chemical and structural drivers for this improvement. Data from our previous characterization-kinetics studies on a CuO-based commercial sorbent (CuO-1)<sup>24,31</sup> are used to compare against the results for the La-CuO sorbents and to demonstrate the effects of La addition on the molecular features of CuO.

## 3.2 | Phyiscochemical properties of La-CuO sorbents identified via nonsynchrotron based techniques

XRD was used to identify the crystalline phases and estimate the average CuO crystal sizes of CuO-1, CuO-LaO-1, and La-Cu-2. The XRD patterns (Figure S3) of the fresh sorbents show diffraction peaks that are characteristic of single-phase monoclinic CuO.<sup>36</sup> Peaks at  $2\theta=29^{\circ}$  and  $42^{\circ}$  in the pattern for CuO-La-1 identify NaNO<sub>3</sub> and indicate that some of the Na precipitated as a solid phase during the sol-gel synthesis. CuO-La-2 showed evidence of minor contributions of the CuLa<sub>2</sub>O<sub>4</sub> phase (Figure S4; 1.8 total wt.% CuLa<sub>2</sub>O<sub>4</sub>), contributing to, but not fully explaining, the higher level of La inclusion in that sample. The average crystal sizes of the sorbents using Rietveld refinement were 16 nm for CuO-La-1, 42 nm for CuO-La-2, and 2.8 for CuO-1 (Figure S4). Rietveld refinement results show that there is strain present in CuO-La-2 (0.13%) and CuO-La-1 (0.30%). The unit cell volume of both CuO-La-1 (81.20 Å<sup>3</sup>) and CuO-La-2 (81.19 Å<sup>3</sup>) also show small expansions as compared to the CuO tenorite structure (81.080 Å<sup>3</sup>). The phase and strain identification from XRD analysis support the conclusion of La incorporation into CuO. As mentioned above, the La-containing samples exhibit higher removal capacities than the CuO sample despite possessing larger CuO crystallites, and according to previous work (both by the authors<sup>23,25</sup> and others<sup>22</sup>), the increase in capacity results from strain induced by lattice expansion. Thus, the addition of La into CuO disrupts the lattice and leads to the increase in H<sub>2</sub>S capacity. Furthermore, the small lattice expansion observed in CuO-La samples may make the conversion from CuO to CuS more facile by reducing CuO lattice energy.

15475905, 2021, 12, Downloaded

from https://aiche.onlinelibrary.wiley.com/doi/10.1002/aic.17484 by Purdue University (West Lafayette), Wiley Online Library on [10/07/2023]. See the Terms

of use; OA articles are governed by the applicable Creati

nm

N<sub>2</sub>-physisorption measurements were performed for the samples (CuO-1, CuO-La-1, and CuO-La-2) to probe their textural properties (Table S2). Both La-CuO sorbents had surface areas that were lower than the commercial sorbent (23  $\mathrm{m^2~g^{-1}}$  for CuO-La-1 and 11  $\mathrm{m^2~g^{-1}}$ for CuO-La-2 compared to  $63 \text{ m}^2 \text{ g}^{-1}$  for CuO-1). On the other hand, CuO-1 and CuO-La-1 exhibited comparable porosities (0.14 and 0.17 cm<sup>3</sup> g<sup>-1</sup> respectively) while CuO-La-2 had a considerably lower porosity of 0.019 cm $^3$  g $^{-1}$ . Thus, BET results suggest that surface area and porosity were not the determining factor for the sorbents' performance, as the sample with lowest porosity, CuO-La-2, achieved the highest removal capacity (35.8 g H<sub>2</sub>S per 100 g CuO). This is consistent with findings in a previous study that concluded that favored textural properties (i.e., small agglomerates in SEM, and larger surface areas and pore volumes) do not necessarily equate to improved performance.23

Moreover, Figure S3 shows the XRD patterns of the spent samples where peaks corresponding to both CuO and CuS were identified. A reduction in the peak intensity and broadening of the CuO reflections were observed for all spent samples due to the conversion of CuO to CuS. The small crystallites of CuO remaining contribute only weak intensity, broad CuO peaks to the XRD pattern. The sulfidation of copper oxide is associated with a unit-cell volume expansion (60%) that disrupts lattice structure of the remaining CuO phase at the CuO-CuS interface.<sup>25</sup> This disruption is likely a critical factor for the overall extent of sulfidation, and explains, in part, the apparent lack of correlation between capacity and textural properties. 22-23

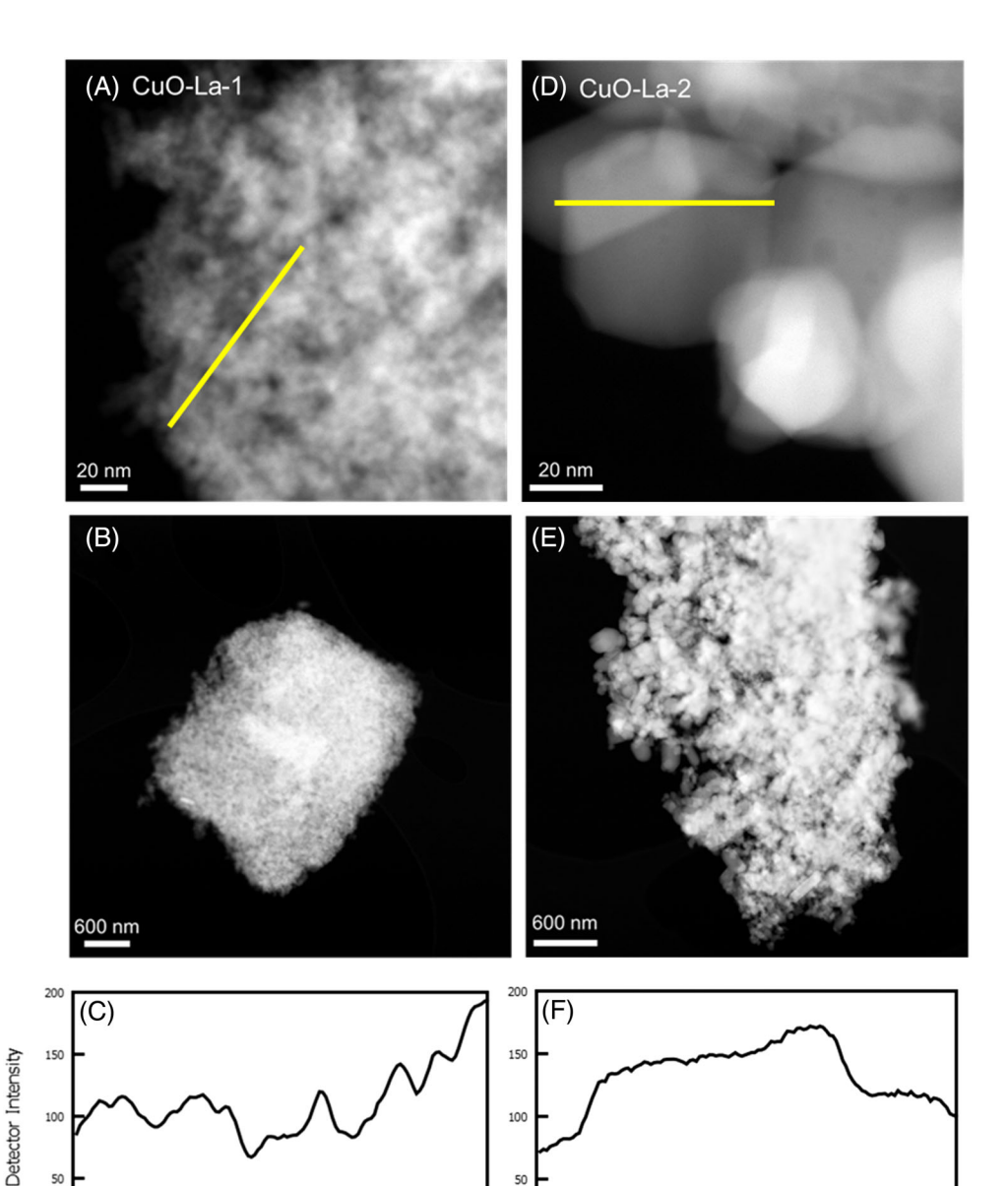


FIGURE 1 STEM images of CuO-La-1 (a-b) and CuO-La-2 (d-e). The detector intensity profiles for CuO-La-1 (c) and CuO-La-2 (f) are generated along the identified vellow lines in the STEM images. The smooth and additive intensity of CuO-La-2 indicates even distribution of the La species, in comparison with the blotchy appearance of Cu-O-La-1 is caused by the smaller crystallites and their superposition to generate variation in signal intensity

100

nm

STEM and TEM images of CuO-La-1 and CuO-La-2 samples are shown in Figure 1. In Figure 1D, the CuO-La-2 particles, of 20–50 nm size, show uniform intensity across the width of each particle. An intensity line profile (Figure 1F) along the yellow line in Figure 1D shows the plateau of intensity across a single particle in the CuO-La-2 sample. CuO-La-1 shows larger variation in intensity over shorter length scales. Both images are representative of the samples and in agreement with crystallite sizes obtained by XRD. Selected area EDS results (Figure S5) show that in any given 100 nm area, La is 3.3  $\pm$  0.3 wt.% for CuO-La-2 sample and 1.0  $\pm$  1.4 wt.% for CuO-La-1. The relatively low variation in the EDS results of the CuO-La-2 sample is consistent with the even intensity of each particle throughout the sample in the STEM images. On the other hand, the high relative deviation of La content in the CuO-La-1 sample suggests some compositional nonuniformity on the 100 nm scale.

In summary, the laboratory-based characterization showed that CuO-La-2, compared to CuO-La-1, features larger crystals but has a higher inclusion of La throughout the CuO phase. These results suggest that the improvement in sulfur uptake by CuO-La-2, compared to CuO-La-1, is related to a higher concentration of La dopants which induce lattice expansion and strain, which have been previously identified as a means to increase  $H_2S$  capacity of CuO adsorbents.  $^{22,23,25}$ 

### 3.3 | Multiedge XAS study of changes in chemical environment

To investigate the structural and chemical changes induced by La addition to CuO sorbents, XAS experiments were performed at each of the Cu K-, S K-, and La  $L_3$ -edges. For the S- and La-edges, XANES spectra were measured, while full EXAFS was measured at the Cu K-

edge. Figure 2 shows the Cu K-edge XANES of the fresh and spent samples: CuO-1, CuO-La-1, and CuO-La-2. Spectra of the fresh samples are qualitatively consistent with CuO XANES in previous studies and XRD results presented above.  $^{37}$  The pre-edge feature at 8979 eV in all three samples arises from a Cu  $1s^2$  to  $3d^9$  dipole forbidden transition. This feature is indicative of  $Cu^{2+}$  species as there are no empty 3d orbitals in the  $Cu^+$  species. Upon addition of La to the CuO, there is an increase in the definition of the pre-edge peak and the white line. The increased pre-edge definition is consistent with the larger CuO crystallites present in the lanthanum containing samples (16 and 40 nm) as compared to the CuO-1 (3 nm).

To quantify the structural differences between La-CuO samples and the reference CuO-1 sample, the Cu K-edge EXAFS of the fresh samples was modeled. The EXAFS best-fit model for all samples, Table S2 and Figures S6–S8, included scattering paths matching hexagonal CuO structure, tenorite, in agreement with the XRD results. It was not possible to model a Cu-La scattering contribution. The first Cu—O scattering path, at  $\approx\!1.95$  Å, was the same, within error, for all samples. Subsequent Cu—Cu and Cu—O scattering paths characterizing the La containing samples were elongated by approximately 0.2 Å compared to the CuO-1 sample. These results indicate an expansion of the packing structure caused by the inclusion of La into the CuO lattice. In turn, this expansion could explain both the unit cell expansion and the origin of the strain measured by XRD, which leads to the observed increases in capacity by reducing reaction barriers for oxygen atoms to reaction with absorbed species derived from  $H_2S.^{23,25}$ 

Figure 2 also shows XANES spectra measured at the Cu K-edge for spent samples after exposure to 1000 ppm-vol  $H_2S$ , 323 K, and 1 atm for 4–6 h. For both La-CuO samples, linear combination analysis using the spectra of tenorite (CuO) and covellite (CuS) as the basis set shows (see Figure S9; Table S3) that approximately 50% of the oxygen

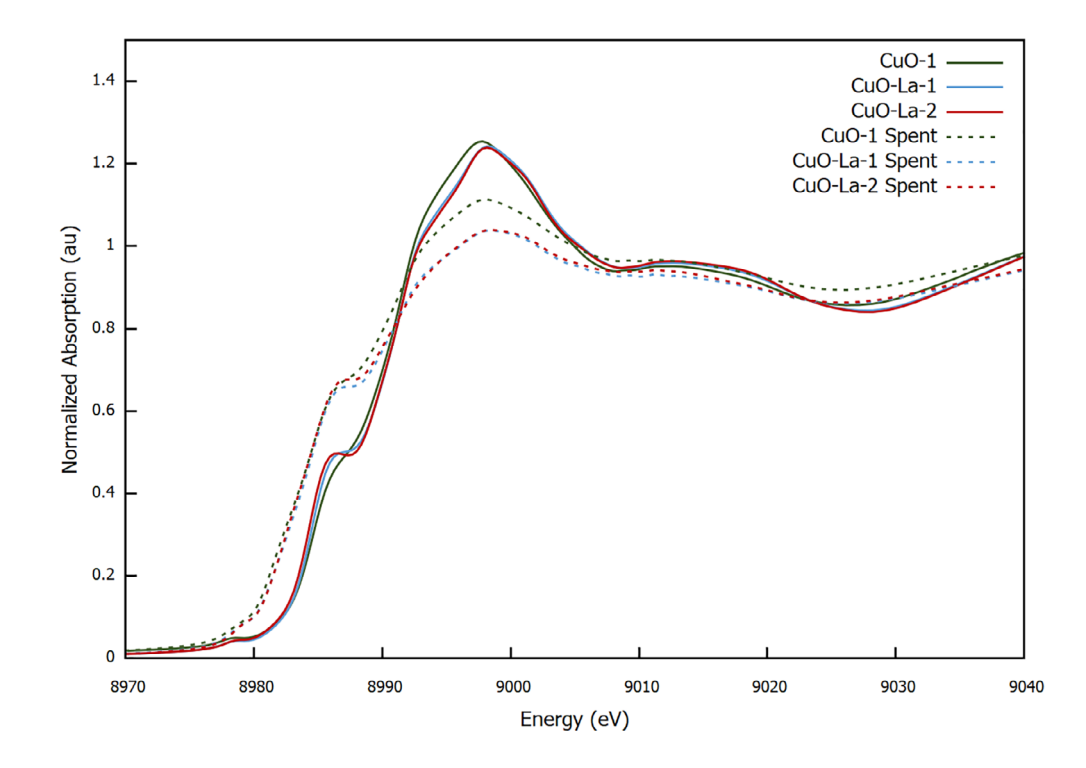


FIGURE 2 Normalized Cu K-edge XANES spectra for the CuO-based sample, CuO-1, and La-CuO samples, CuO-La-1 and CuO-La-2. Curves shown include the as-prepared and spent material after sulfidation

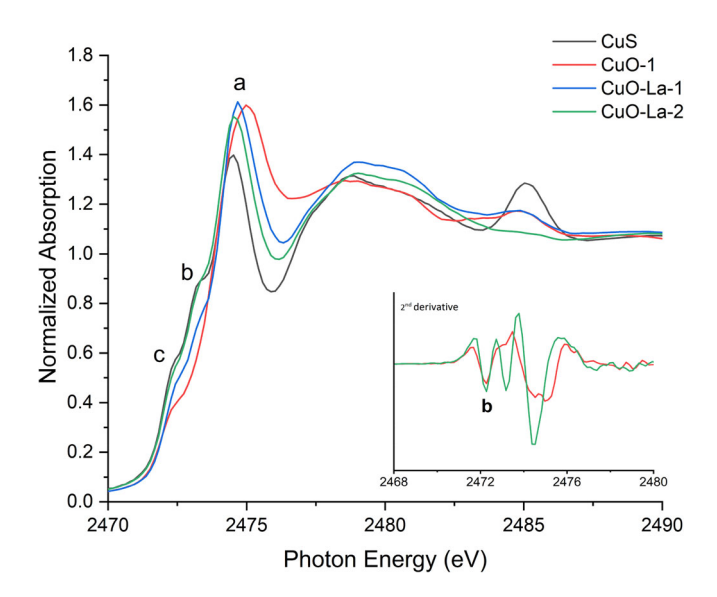


FIGURE 3 Normalized S K-edge XANES spectra for CuO-1, CuO-La-1, CuO-La-2 spent at 323 K, 1 atm, and 1000 ppm-vol H<sub>2</sub>S/He and a covellite reference (CuS). The inset shows the second derivative spectra of the CuO-1 and CuO-La-2 spent samples highlighting the presence of peak b ( $S_2^{2-}$  1s  $\rightarrow$  Cu<sup>2+</sup> 3d<sup>9</sup>) in the spent CuO-La-2 which indicates higher conversion and CuS-like products

had been replaced by sulfur during these in situ experiments. For the CuO-La-1, this is the upper limit of sulfur uptake determined from fixed-bed experiments. Again, these spectra show a blue-shifted white line peak relative to the CuO sample. However, in contrast to the fresh samples, the white line is attenuated relative to that of spent CuO-1 sample, which is indicative of a more electron-rich Cu species in the spent material. The absence of a strong peak at 8980 eV (characteristic of Cu<sub>2</sub>S) in the spent samples, indicates that Cu<sup>+</sup>-S<sup>-2</sup> species are not formed in this reaction.38

At the S K-edge, ex situ XANES spectra were collected for spent CuO-1, CuO-La-1, and CuO-La-2 under He flow, after sulfidation at 1000 ppm-vol H<sub>2</sub>S/He, 323 K, and 1 atm (Figure 3). Previous work on the XANES region of the S K-edge has highlighted its ability to provide information on the oxidation state of sulfur in the sample, following the general trend that the white line maxima is shifted to higher energy with increased sulfur oxidation state (peak a in Figure 3).<sup>39,40</sup> This indicates that, in comparison to CuO-1, the La-CuO samples possess sulfur species which are more electron rich.

Another important spectral feature that speciates the type of copper sulfide present are the pre-edge peaks at 2469.9 eV (c) and 2470.7 eV (b) in Figure 3. These features correspond to  $S^{2-}$  1s  $\rightarrow$  Cu<sup>2+</sup>  $3d^9$  and  $S_2^{2-}$  1s  $\rightarrow$   $Cu^{2+}$   $3d^9$  transitions, respectively.<sup>25,41</sup> Figure 3 shows that the S K-edge spectra of both spent La-CuO samples and CuS reference contain both pre-edge features, while peak (b) is absent in the spent CuO-1 spectra. This difference is more apparent in the second derivative plots of CuO-1 and CuO-La-2 spectra (inset of Figure 3). In a study that speciates the results of sulfidation of CuO at different temperatures, 41 the absence of peak b was associated with the formation of distorted CuS species at the interface of CuO/CuS which dominates the spectra at low conversions of CuO to CuS, where most of the

CuS is at grain boundaries. CuO samples that achieve higher conversion exhibit higher intensity of peak b at 2470.7 eV in their K-edge XANES spectra which is consistent with the spectral features of bulk covellite, as the core of the CuO crystallites has been converted to CuS. These observations are consistent with the extent of conversion of these samples CuO-1 (59%) CuO-La-1 (64%) and CuO-La-2 (85%) and their crystallite sizes. For CuO-1, the lack of peak b shows that most of the CuS formed is in interfacial regions such as grain boundaries. Despite a similar extent of sulfidation, CuO-La-1 shows peak b because much of the CuS is in the bulk of the crystallites rather than grain boundaries. Finally, the presence of a peak at 2482-2483 eV in all samples (except CuO-La-2) indicates the presence of trace  $SO_4^{2-}$ , likely in the form of copper sulfate.<sup>39</sup> This is the result of some partial oxidation of the samples in air prior to running these scans and not a fundamental difference in reaction mechanism. The presence of the same peak in the CuS covellite reference confirms this assumption.

The similarity between CuO-La-1 and CuO-La-2 XANES at the Cu and S K-edges shows that the difference in performance between the two samples is not due to a difference in the form of sulfide products, but rather results from higher concentration of La in CuO-La-2. On the other hand, the difference between the XANES of both La-CuO samples and CuO-1 indicates that the improvement of sulfur uptake upon lanthanum addition to CuO has an electronic component, in addition to the structural changes shown by EXAFS and XRD.

Finally, XANES spectra taken at the La L<sub>3</sub>-edge show that, in comparison to CuO-La-1 and La<sub>2</sub>O<sub>3</sub> reference, CuO-La-2 sample shows a less intense and broadened white line (Figure 4). This broadening is characteristic of a decrease in La-O coordination.<sup>42</sup> This observation can be interpreted to be a result of the more uniform atomic distribution of La in the CuO phase for CuO-La-2 sample, as La in this environment has a lower La-O coordination number than that of La<sub>2</sub>O<sub>3</sub>. This is consistent with the EDS results suggesting higher percentage of La in this sample and lower variations of La concentration from spot to spot. Nevertheless, after reaction, both La-CuO samples exhibit overlapping La L3-edge spectra suggesting similar La environment in the spent samples. With the high conversion of Cu-La-2 sample (85%) the average La-O coordination number increases. This may be due to a restructuring of the local environment around dispersed La atoms upon formation of CuS.

#### Reaction kinetics using in situ XAS and fixed-3.4 bed experiments

Fixed-bed sorption experiments were conducted to determine removal kinetics at 1000 ppm-vol H<sub>2</sub>S/N<sub>2</sub>, 323 K, and 1 atm. The breakthrough curves of effluent H<sub>2</sub>S concentration were then fit using a linear driving force model (Equations S1-S5)31,43 to quantify the sulfidation kinetics in terms of a first order rate parameter, k. The experiments were run under conditions that eliminate external and macro/mesopore diffusion such that k reflects the rate of H<sub>2</sub>S uptake at the crystallite scale.<sup>31</sup> Figure S10 shows the breakthrough curves for CuO-1, CuO-La-1, and CuO-La-2

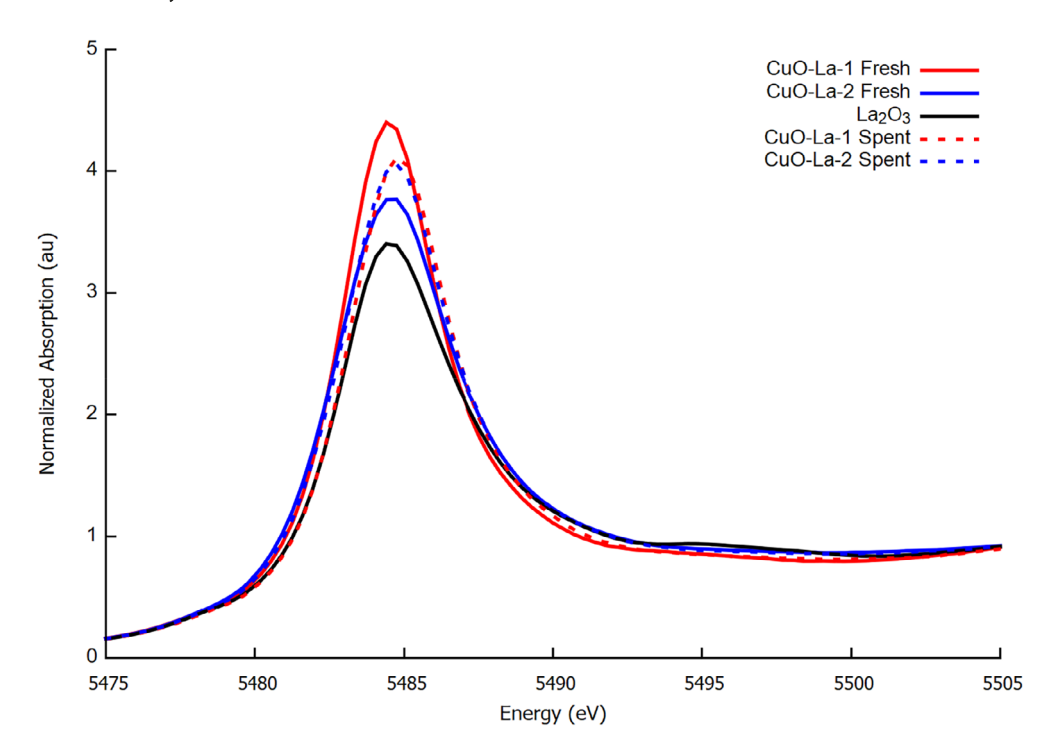


FIGURE 4 Normalized L<sub>3</sub>-edge XANES spectra for CuO-La-1, CuO-La-2 both fresh and spent at 323 K, 1 atm, and 1000 ppm-vol H<sub>2</sub>S/He and a lanthanum oxide reference (La<sub>2</sub>O<sub>3</sub>)

**TABLE 1** Summary of rate parameters deduced from cooper model fit, removal capacity, and conversion of CuO for fixed-bed sorption tests at 1000 ppm-vol H<sub>2</sub>S/N, 323 K, and 1.0 atm

Sample	k (s <sup>-1</sup> )	q <sub>s</sub> (g H <sub>2</sub> S per 100 g sorbent)	Conversion (%)
CuO-1	18 ± 2	24.9	59
CuO-La-1	22 ± 1	26.9	64
CuO-La-2	7.4 ± 0.8	35.8	85

**TABLE 2** Random pore model parameters from fits of the conversion profiles of S K-edge *in situ* sulfidation runs at 1000 ppm-vol H<sub>2</sub>S/N, 323 K and 1.0 atm

Sample	$k \times 10^3  (\mathrm{cm^4  mol^{-1}  s^{-1}})$	$D  imes 10^{12}  (\text{cm}^2  \text{s}^{-1})$
CuO-1	6.0 ± 1.6	2.3 ± 1.1
CuO-La-1	2.6 ± 0.2	5.4 ± 1.7
CuO-La-2	0.71 ± 0.08	17 ± 3

experiments, normalized for inlet  $H_2S$  concentration, along with the model fits (black solid lines). Table 1 summarizes k,  $q_{\rm S}$ , and CuO conversion for each material. As mentioned in Section 3.1, fixed-bed results show that CuO-La-1 and CuO-La-2 samples achieved  $q_{\rm S}$  values of 26.9 and 35.8 g  $H_2S$  per 100 g CuO, respectively. Analysis of the breakthrough curves (Figure S10) show that the material achieving the highest capacity (CuO-La-2) exhibits the smallest apparent rate parameter (7.4 s $^{-1}$ : Table 1).

In situ XAS experiments at the S K-edge were also run to quantify the  $H_2S$  removal kinetics of these materials. The S K-edge spectra show changes from  $H_2S$  like features, in the first few scans, to CuS like features as the reaction progresses (Figure S11). The edge steps for the

scans were used to deduce the amount of sulfur in the sample at each point in time, where the maximum conversion from fixed-bed experiments was assumed to correspond to the edge step for the spent sample from in situ XAS experiments. The contribution of gaseous  $\rm H_2S$  spectra, determined from the difference between spent sample spectra under  $\rm H_2S$  and under He flow, was subtracted from all spectra prior to analysis. The conversion profiles for the three samples, as determined from sulfur content, are shown in Figure S12, while Table 2 summarizes the rate constants and effective diffusivities derived from random pore model (RPM) fits of the data (Equations S6–S10). $^{44,45}$ 

Similar to the trends observed in fixed-bed experiments, the rate parameters for CuO-1 ( $6.3 \times 10^{-3} \text{ cm}^4 \text{ mol}^{-1} \text{ s}^{-1}$ ) and CuO-La-1 ( $2.6 \times 10^{-3} \text{ cm}^4 \text{ mol}^{-1} \text{ s}^{-1}$ ) were larger than the CuO-La-2 rate parameter ( $7.1 \times 10^{-4} \text{ cm}^4 \text{ mol}^{-1} \text{ s}^{-1}$ ). This trend can be observed in the initial region of the conversion profiles, Figure S12, with the most rapid change in conversion for CuO-1, followed by CuO-La-1 and then, CuO-La-2. This initial rapid change in conversion, however, results in a shorter reaction-controlled regime for CuO-1 (20 min) compared to CuO-La-1 (55 min) and CuO-La-2 (125 min). In addition, CuO-La-2 (17  $\times 10^{-12} \text{ cm}^2 \text{ s}^{-1}$ ) exhibited the highest effective diffusivity in the diffusion-controlled regime, despite possessing the lowest initial porosity (0.019 cm³ g<sup>-1</sup>; Table S4), thereby allowing this sorbent to continue to remove H<sub>2</sub>S at a higher rate than CuO-1 (2.3  $\times 10^{-12} \text{ cm}^2 \text{ s}^{-1}$ ) and CuO-La-1 (5.4  $\times 10^{-12} \text{ cm}^2 \text{ s}^{-1}$ ).

### 4 | CONCLUSION

In conclusion, a combination of conventional and synchrotron-based characterization methods allowed us to study the chemical and structural changes induced by the introduction of La to CuO sorbents, and

AIChE 9 of 10 curation (equal); formal analysis (equal); writing - original draft (equal); writing - review and editing (equal). Alexey Boubnov: Data curation (equal). Faisal Alshafei: Data curation (equal). Richa Ghosh: Data curation (equal). Brian Ko: Data curation (equal). Abhaya Datye: Formal analysis (equal); writing - original draft (equal); writing review and editing (equal). Simon Bare: Conceptualization (equal); Formal analysis (equal); writing - original draft (equal); writing review and editing (equal). Dante Simonetti: Conceptualization (equal); funding acquisition (lead); project administration (lead); writing - original draft (equal); writing - review and editing (equal). **CONFLICT OF INTEREST** The authors declare no conflict of interest. ASSOCIATED CONTENT Details of experimental methods, model derivations, and additional this article via a link at the end of the document.

the correlation between these changes and the enhanced performance of the sorbents. La-containing sorbents, of similar bulk La content, prepared via different synthesis methods: sol-gel and coprecipitation with ammonium, yielded materials with different physiochemical properties and sulfur removal performance. Both samples achieved improved sulfur removal capacities despite having larger crystallite sizes and smaller surface area compared to CuO sorbents. This improved removal capacity was associated with slower rate parameters (both in fixed-bed reactor and under gradient-less conditions during in situ XAS) compared to CuO-based reference sorbent. The slower rates allowed for an extended reaction-controlled regime which resulted in improved conversion. Cu K-edge EXAFS fits for the samples revealed that the introduction of La distorted Cu(-O)4 unit packing, evident by the elongation of this scattering path along with third and fourth shell Cu-Cu single scatterings. Cu K-edge XANES also revealed a more electron-rich environment for Cu in La-doped samples which makes the Cu-O bond more susceptible to breaking and, thus, more reactive toward sulfur. The La L<sub>3</sub>-edge results revealed lower coordination of La-O in the coprecipitation sample, CuO-La-2, compared to the sol-gel sample, CuO-La-1, and bulk La<sub>2</sub> O<sub>3</sub> reference, which is consistent with the higher content of La in CuO phase that was determined by STEM-EDS. In addition to higher La inclusion, uniform dispersion of La within CuO phase allowed for higher Cu-La interaction and, thus, better performance improvement. Taken together, these results show that La doping improves the sulfidation performance by disrupting the CuO lattice resulting in strain that lowers energy barriers for oxygen atoms to form vacancies via hydroxyl group formation and migration. 23,25

### **ACKNOWLEDGMENTS**

The authors acknowledge financial support from the UCLA Samueli School of Engineering, the Office of Equity, Diversity, and Inclusion at UCLA, and the donors of The American Chemical Society Petroleum Research Fund for partial support of this research. Use of the SSRL, SLAC National Accelerator Laboratory, and Co-ACCESS are supported by the U.S. Department of Energy, Office of Science, Office of Basic Energy Sciences under Contract No. DE-AC02-76SF00515. This work was performed, in part, at the Center for Integrated Nanotechnologies, an Office of Science User Facility operated for the U.S. Department of Energy (DOE) Office of Science by Los Alamos National Laboratory (Contract 89233218CNA000001) and Sandia National Laboratories (Contract DE-NA-0003525). Additional funding was provided from the U.S. National Science Foundation grant EEC-1647722 (CISTAR). The authors acknowledge Luke Minardi's assistance in N<sub>2</sub> physisorption data collection. Griffin A. Canning would like to thank E. J. Peterson for his guidance with the Rietveld refinement.

### **AUTHOR CONTRIBUTIONS**

Griffin Canning: Data curation (equal); formal analysis (equal); writing original draft (equal); writing - review and editing (equal). Sara Azzam: Data curation (equal); formal analysis (equal); writing - original draft (equal); writing - review and editing (equal). Adam Hoffman: Data

characterization results are available in the Supporting Information for

### **DATA AVAILABILITY STATEMENT**

The data that support the findings of this study are openly available upon request from the corresponding author(s).

#### ORCID

Dante A. Simonetti https://orcid.org/0000-0002-5708-460X

### REFERENCES

- 1. Cozzi L. Total primary energy demand in the new policy scenario. Accessed August 18, 2019. https://www.iea.org/weo/
- 2. Cui H, Turn SQ, Reese MA. Removal of sulfur compounds from utility pipelined synthetic natural gas using modified activated carbons. Catal Today. 2009;139(4):274-279. doi:10.1016/j.cattod.2008.03.024
- 3. Kidnay AJ, Parrish W. Fundamentals of Natural Gas Processing. CRC Press: 2006.
- 4. Haouzi P, Sonobe T, Judenherc-Haouzi A. Developing effective countermeasures against acute hydrogen sulfide intoxication: challenges and limitations: treatment of sulfide poisoning. Ann N Y Acad Sci. 2016;1374(1):29-40. doi:10.1111/nyas.13015
- 5. LNG a Nontechnical Guide (Tusiani, Shearer). Natural Gas. Liquefied Natural Gas. Accessed August 18, 2019. https://www.scribd.com/ document/346110931/LNG-a-Nontechnical-Guide-Tusiani-Shearer
- 6. Goodwin MJ, Musa OM, Steed JW. Problems associated with sour gas in the oilfield industry and their solutions. Energy Fuel. 2015;29(8): 4667-4682. doi:10.1021/acs.energyfuels.5b00952
- 7. Kulprathipanja S. Zeolites in Industrial Separation and Catalysis. Wiley-VCH: 2010.
- 8. Ruthven DM. Principles of Adsorption and Adsorption Processes. Wiley; 1984.
- 9. Samokhvalov A, Tatarchuk BJ. Characterization of active sites, determination of mechanisms of H<sub>2</sub>S, COS and CS<sub>2</sub> sorption and regeneration of ZnO low-temperature sorbents: past, current and perspectives. Phys Chem Chem Phys. 2011;13(8):3197-3209. doi:10.1039/C0CP01227K
- 10. Samokhvalov A, Tatarchuk B. Review of experimental characterization of active sites and determination of molecular mechanisms of adsorption, desorption and regeneration of the deep and ultradeep desulfurization sorbents for liquid fuels. Catal Rev. 2010;52(3): 381-410.

- Rosso I, Galletti C, Bizzi M, Saracco G, Specchia V. Zinc oxide sorbents for the removal of hydrogen sulfide from syngas. *Ind Eng Chem Res.* 2003;42(8):1688-1697. doi:10.1021/ie0208467
- 12. Garces HF, Galindo HM, Garces LJ, Hunt J, Morey A, Suib SL. Low temperature  $H_2S$  dry-desulfurization with zinc oxide. *Microporous Mesoporous Mater.* 2010;127(3):190-197. doi:10.1016/j.micromeso. 2009 07 022
- Balichard K, Nyikeine C, Bezverkhyy I. Nanocrystalline ZnCO<sub>3</sub>—a novel sorbent for low-temperature removal of H<sub>2</sub>S. J Hazard Mater. 2014;264:79-83. doi:10.1016/j.jhazmat.2013.10.068
- Girard V, Baudot A, Chiche D, Bazer-Bachi D, Bounie C, Geantet C. Rational selection of single oxide sorbents for syngas desulfurization regenerable at reduced temperature: thermochemical calculations and experimental study. *Fuel.* 2014;128:220-230. doi:10.1016/j.fuel. 2014.02.058
- Rosenqvist T. Phase equilibria in the pyrometallurgy of sulfide ores. Metall Trans B. 1978;9(3):337-351. doi:10.1007/BF02654407
- Kyotani T, Kawashima H, Tomita A. High-temperature desulfurization with copper-containing sorbents. *Environ Sci Technol.* 1989;23(2): 218-223. doi:10.1021/es00179a014
- Tamhankar SS, Bagajewicz M, Gavalas GR, Sharma PK, Flytzani-Stephanopoulos M. Mixed-oxide sorbents for high-temperature removal of hydrogen sulfide. *Ind Eng Chem Process Des Dev.* 1986; 25(2):429-437. doi:10.1021/i200033a014
- Elyassi B, Wahedi YA, Rajabbeigi N, et al. A high-performance adsorbent for hydrogen sulfide removal. *Microporous Mesoporous Mater*. 2014;190:152-155. doi:10.1016/j.micromeso.2014.02.007
- 19. Huang G, He E, Wang Z, et al. Synthesis and characterization of  $\gamma$ -Fe<sub>2</sub> O<sub>3</sub> for H<sub>2</sub>S removal at low temperature. *Ind Eng Chem Res.* 2015; 54(34):8469-8478. doi:10.1021/acs.iecr.5b01398
- Baird T, Campbell KC, Holliman PJ, Hoyle R, Stirling D, Williams BP. Mixed Co-Zn-Al oxides as absorbents for low-temperature gas desulfurisation. J Chem Soc Faraday Trans. 1995;91(18):3219-3230. doi: 10.1039/FT9959103219
- Xue M, Chitrakar R, Sakane K, Ooi K. Screening of adsorbents for removal of H<sub>2</sub>S at room temperature. *Green Chem.* 2003;5(5):529-534. doi:10.1039/B303167P
- Polychronopoulou K, Fierro JLG, Efstathiou AM. Novel Zn-Ti-based mixed metal oxides for low-temperature adsorption of H<sub>2</sub>S from industrial gas streams. Appl Catal B Environ. 2005;57(2):125-137.
- Azzam SA, Alshafei FH, López-Ausens T, et al. Effects of morphology and surface properties of copper oxide on the removal of hydrogen sulfide from gaseous streams. *Ind Eng Chem Res.* 2019;58(40):18836-18847. doi:10.1021/acs.iecr.9b03975
- Hoffman AS, Azzam S, Zhang K, et al. Direct observation of the kinetics of gas-solid reactions using in situ kinetic and spectroscopic techniques. React Chem Eng. 2018;3(5):668-675. doi:10.1039/C8RE00020D
- Azzam S, Boubnov A, Hoffman AS, et al. Insights into copper sulfide formation from cu and S K-edge XAS and DFT studies. *Inorg Chem.* 2020;59:15276-15288.
- Grant DJW, York P. A disruption index for quantifying the solid state disorder induced by additives or impurities. II. Evaluation from heat of solution. *Int J Pharm.* 1986;28(2–3):103-112. doi:10.1016/0378-5173 (86)90233-4
- Sun X-Y, Zhang X, Sun X, Qian N-X, Wang M, Ma Y-Q. Improved adsorption and degradation performance by S-doping of (001)-TiO<sub>2</sub>. Beilstein J Nanotechnol. 2019;10:2116-2127. doi:10.3762/bjnano.10.206
- Polychronopoulou K, Galisteo FC, Granados ML, Fierro JLG, Bakas T, Efstathiou AM. Novel Fe-Mn-Zn-Ti-O mixed-metal oxides for the low-temperature removal of H<sub>2</sub>S from gas streams in the presence of H<sub>2</sub>, CO<sub>2</sub>, and H<sub>2</sub>O. J Catal. 2005;236(2):205-220.
- Kayani ZN, Umer M, Riaz S, Naseem S. Characterization of copper oxide nanoparticles fabricated by the sol-gel method. *J Electron Mater.* 2015;44(10):3704-3709. doi:10.1007/s11664-015-3867-5

- Singhal S, Kaur J, Namgyal T, Sharma R. Cu-doped ZnO nanoparticles: synthesis, structural and electrical properties. *Phys B Condens Matter*. 2012;407(8):1223-1226. doi:10.1016/j.physb.2012.01.103
- Azzam S, Simonetti DA. Linear driving force approximations as predictive models for reactive sorption. *Energ Technol*. 2019;8:1900718. doi:10.1002/ente.201900718
- Petford-Long AK, Long NJ. Safe limits for electron beam analysis of copper oxides. *Ultramicroscopy*. 1990;34:27-32.
- Bolin TB, Wu T, Schweitzer N, et al. In situ intermediate-energy X-ray catalysis research at the advanced photon source beamline 9-BM. Catal Today. 2013;205:141-147. doi:10.1016/j.cattod.2012.09.034
- Ravel B, Newville M. ATHENA, ARTEMIS, HEPHAESTUS: data analysis for X-ray absorption spectroscopy using IFEFFIT. J Synchrotron Radiat. 2005;12(4):537-541. doi:10.1107/S0909049505012719
- Inorganic Crystal Structure Database ICSD | FIZ Karlsruhe.
  Accessed August 31, 2019. https://www.fiz-karlsruhe.de/de/produkte-und-dienstleistungen/inorganic-crystal-structure-database-icsd
- Åsbrink S, Norrby LJ. A refinement of the crystal structure of copper(II) oxide with a discussion of some exceptional e.s.d.'s. Acta Crystallogr B. 1970;26(1):8-15. doi:10.1107/S0567740870001838
- Sharma A, Varshney M, Park J, Ha T-K, Chae K-H, Shin H-J. XANES, EXAFS and photocatalytic investigations on copper oxide nanoparticles and nanocomposites. RSC Adv. 2015;5(28):21762-21771.
- Lamberti C. The use of synchrotron radiation techniques in the characterization of strained semiconductor Heterostructures and thin films. Surf Sci Rep. 2004;53(1–5):1-197. doi:10.1016/j.surfrep. 2003.12.001
- Pickering IJ, Prince RC, Divers T, George GN. Sulfur K-edge X-ray absorption spectroscopy for determining the chemical speciation of sulfur in biological systems. FEBS Lett. 1998;441(1):11-14. doi:10. 1016/S0014-5793(98)01402-1
- Fleet ME, Liu X, Harmer SL, King PL. Sulfur K-edge XANES spectroscopy: chemical state and content of sulfur in silicate glasses. *Can Mineral*. 2005;43(5):1605-1618. doi:10.2113/gscanmin.43.5.1605
- 41. Kumar P, Nagarajan R, Sarangi R. Quantitative X-ray absorption and emission spectroscopies: electronic structure elucidation of  $Cu_2S$  and CuS. J Mater Chem C. 2013;1(13):2448-2454. doi:10.1039/c3tc00639e
- 42. Asakura H, Shishido T, Teramura K, Tanaka T. Local structure and La L1 and L3-edge XANES spectra of lanthanum complex oxides. *Inorg Chem.* 2014;53(12):6048-6053. doi:10.1021/ic500381z
- 43. Cooper RS. Slow particle diffusion in ion exchange columns. *Ind Eng Chem Fund*. 1965;4(3):308-313. doi:10.1021/i160015a012
- Bhatia SK, Perlmutter DD. A random pore model for fluid-solid reactions: I. Isothermal, kinetic control. AIChE J. 1980;26(3):379-386. doi: 10.1002/aic.690260308
- Bhatia SK, Vartak BJ. Reaction of microporous solids: the discrete random pore model. *Carbon*. 1996;34(11):1383-1391. doi:10.1016/ S0008-6223(96)00080-2

### SUPPORTING INFORMATION

Additional supporting information may be found in the online version of the article at the publisher's website.

**How to cite this article:** Canning GA, Azzam SA, Hoffman AS, et al. Lanthanum induced lattice strain improves hydrogen sulfide capacities of copper oxide adsorbents. *AIChE J.* 2021; 67(12):e17484. doi:10.1002/aic.17484